PFS/MEX limb observations of 4.3-μm CO_2 non-LTE emission in the atmosphere of Mars

M. Giuranna[1], S. Fonte[1], A. Longobardo[1], G. Sindoni[1], P. Wolkenberg[1,2] and V. Formisano[†]

[1]Istituto di Astrofisica e Planetologia Spaziali (IAPS). Istituto Nazionale di Astrofisica (INAF), Via del Fosso del Cavaliere 100, Rome, 00133, Italy
[2]Centrum Badan Kosmicznych Polska Akademia Nauk, ul. Bartycka 18a, Warsaw, Poland

07 March, 2018

Revised manuscript submitted to *Icarus*

Number of pages: 42
Number of tables: 1
Number of figures: 11

Proposed Running Head:

PFS/MEX non-LTE limb observations

Keywords:

Mars; Mars, atmosphere; Atmospheres, structure; Atmospheres, Non-LTE

Please send Editorial Correspondence to:

Marco Giuranna
Istituto di Astrofisica e Planetologia Spaziali INAF-IAPS,
Via del Fosso del Cavaliere, 100
00133 - Roma
ITALY
Phone: +39 06 45488 154
E-mail address: marco.giuranna@iaps.inaf.it

ABSTRACT

We present PFS-MEX limb observations of the CO_2 non-local thermodynamic equilibrium (non-LTE) emission at 4.3 μm in the atmosphere of Mars collected in more than six Martian years. With unprecedented spatial and temporal coverage, and relatively high spectral resolution, this unique dataset promises to improve our understanding of the upper atmosphere of Mars. The former allows analyses of the emission as a function of tangent altitude, solar zenith angle, season, latitude, local time, and thermal condition of the atmosphere. The latter allows unambiguous identification of several emission bands of different isotopologues. We selected observations in the altitude range 50-200 km.

No emission was detected for altitudes higher than 170 km. The spectral shape of the non-LTE emission changes dramatically with the altitude of the tangent point, reflecting the different contribution of the major and minor CO_2 bands and isotopologues to the total emission at different heights. For altitudes higher than 130 km the observed spectrum is dominated by the second hot (SH) bands of the main isotopologue $^{12}C^{16}O_2$ (also referred to as 626 SH). At lower altitudes, the contribution of the isotopic $^{13}C^{16}O_2$ second hot bands (636 SH) to the observed spectrum gradually increases, and is maximum around 70-80 km. Similar consideration apply to the fourth hot bands of the $^{12}C^{16}O_2$ (626 FRH), and particularly those from the (2001x) levels, whose contribution is maximum around 80-90 km. The 626 SH bands can be observed up to an altitude 160-170 km, and their emission is peaked around 120-130 km. The 626 FRH and 636 SH bands are not observed above 130-140 km. Both the first hot (FH) and the fundamental band (FB) of the main isotopologue show a peculiar behavior. Indeed, these emissions can be observed at all altitudes, from 50 km up to 170 km. The intensity of the FH band increases linearly with decreasing height, while the intensity of the FB band is essentially constant at all altitudes, and rapidly decreases above 150 km.

For a fixed altitude, the solar zenith angle (SZA) is the main parameter affecting the intensity and the spectral shape of the non-LTE emission. For SZA between 0 and 40 degrees the intensity of the emission does not show significant variations. For SZAs larger than 40° the observed emission decreases rapidly with increasing SZA, following a cosine-like relation. The different illumination also affects the spectral shape of the non-LTE emission spectrum. High incidence angles tend to increase the relative contribution of weaker bands compared to stronger/optically thicker bands. For a fixed SZA, we found variation of the intensity of the emission with local time, in response to variations of the thermal structure of the atmosphere.

Latitudinal variation of the intensity of the CO_2 non-LTE are also investigated. The maximum intensity is observed around the sub-solar latitudes, where the solar flux is maximum. The intensity of the emission and the altitude at which the maximum emission is observed also changes with the season. The altitude where the maximum intensity of the 626 SH bands is observed decreases from 120-130 km at the perihelion (Ls=251°), down to ~85 km at the southern winter solstice (Ls = 90°). This is explained by the variability of the thermal structure (scale heights) of the Martian atmosphere with the season, as a response to the changing solar flux. The altitude of a given pressure level depends on the thermal structure of the atmosphere which, in turn, depends on the season. On the contrary, the pressure level of the peak emission does not depend on the scale heights, as it is mainly controlled by the CO_2 column density above the peak.

These results, while on one hand confirm and provide more insights and constraints to some aspects of the non-LTE processes on Mars, on the other hand further stimulate and challenge current theoretical models, possibly bringing closer the moment in which the measurements could be inverted to derive important information about the upper mesosphere and lower thermosphere of Mars.

1 - Introduction

Non Local Thermodynamic Equilibrium (non-LTE) processes play a key role in the cooling and heating rate of the mesosphere and lower thermosphere of Mars. The knowledge of this mechanism is extremely important for the study of the upper atmospheric layers, and it may also affect the lower part of the atmosphere. Indeed, the meteorological processes on Mars, unlike the Earth, appear to have a considerably larger vertical extension, probably involving the top of the neutral atmosphere up to 120 km (Bertaux et al. 2006).

At these altitudes the radiative budget of the atmosphere is determined by the direct absorption of sunlight in the near-IR region between 1 and 5 micron and the cooling via non-LTE emission of the 15-µm CO_2 bands (López-Puertas and López-Valverde, 1995). Particularly important is the absorption of the solar radiation in the range 1.2 - 2.7 µm because a major part of this energy is reemitted in cascade at 4.3 µm and 10 µm (Lopez-Puertas and Taylor, 2001). Vibrational- vibrational (V-V) collisions – where vibrational quanta are exchanged between the colliding molecules – redistribute the absorbed solar energy in a variety of vibrational states (Lopez-Puertas and Taylor, 2001). Collisions occur preferentially between excited and ground state CO_2 molecules rather than between two molecules in an excited state because the population of the carbon dioxide ground state is larger. V-V collisions involve both the major and minor CO_2 isotopes (Lopez-Puertas and Taylor 2001), therefore the contribution of higher order, weak isotopic transitions becomes important. These processes need to be understood in details in order to perform meaningful simulations of the radiative balance of the middle and upper atmosphere of Mars and to extend the present parameterizations of the infrared radiative cooling/heating currently in use in Martian Global Circulation Models (GCMs).

An accurate analysis of the non-LTE emissions requires the combined solution of the problem of ro-vibrational relaxation for a large number of excited vibrational states of CO_2 and CO isotopic molecules, and the radiative transfer equation for a very large number of ro-vibrational lines. To test the available theoretical tools, a complete dataset of observations of the upper Martian atmosphere is extremely important. However, only a few studies of the non-LTE behavior of CO_2 in the mesosphere and thermosphere of Mars exist so far. CO_2 fluorescence emission at 4.3 µm has been observed with the Infrared Space Observatory (ISO) (Lellouch et al.

2000) and it had been suggested to be originated by excited vibrational transitions involving the CO_2 second hot (SH) band. A more detailed study of the CO_2 non-LTE emission at 10 μm has been performed by Maguire et al. (2002) with the Thermal Emission Spectrometer (TES) onboard Mars Global Surveyor (MGS). Limb spectral measurements of the upper atmosphere provided a global map of the 10 μm non-LTE emission up to an altitude of 120 km for the different seasonal periods. Theoretical calculations of the CO_2 atmospheric emissions at 10 μm in the upper atmospheres of Mars and Venus have been performed by Lopez-Valverde et al. (2011a).

Observations of non-LTE radiation at 4.3 μm were carried out with the Planetary Fourier Spectrometer (PFS, Formisano et al. 2005a) and the Observatoire pour la Minéralogie, l'Eau, les Glaces et l'Activité (OMEGA, Bibring et al., 2004) onboard the Mars Express (MEx) mission. Early PFS nadir and limb measurements were used for a first validation test of the non-LTE model (Formisano et al., 2005b; Lopez-Valverde et al., 2005, Gilli et al., 2011), confirming that the main contribution to the spectrum was originated by the emission of the second hot bands of the main CO_2 isotope. PFS limb observations of two case orbits have been discussed by Formisano et al. (2006). The authors detected several emitting bands in the PFS spectra, including the second hot band for the 626 and 636 molecule, and other unidentified minor bands or lines observed for the first time on Mars. PFS observations also indicated that both the intensity and the height of peak emission varies with latitude (Formisano et al. 2006). Similar results have been recently reported by OMEGA observations (Piccialli et al., 2016) and strong non-LTE CO and CO_2 daytime limb emissions were also observed on Venus by the Visible and Infrared Thermal Imaging Spectrometer (VIRTIS) on board the European Venus Express mission (Gilli et al., 2009, 2015).

The advantage of limb measurements is twofold. First, they allow to locate the height above the surface where the non-LTE emission occurs. Second, it is possible to detect the emission from weaker transitions compared to the nadir data, which are useful to put more stringent constraints on the model. Indeed, Formisano et al. (2006)

reported the detection of isotopic bands in addition to the CO_2 SH bands, and a variability of the emission spectra as a function of the altitude of the tangent point. The SH bands dominate the spectra at high altitudes. However, to date, several features observed in the spectra still remain unidentified, especially in the 2280-2310 cm^{-1} spectral region. The identification of all the weak and isotopic bands still requires more observations and detailed theoretical work. High signal to noise ratio (SNR) and spectral resolution observations are essential to validate our theoretical understanding of the non-LTE processes in the upper atmosphere, and to improve the available models, which still fail to quantitatively reproduce the observed emission spectra of terrestrial planets (Lopez-Valverde et al., 2011b). We here extend the analysis of the main characteristics of the 4.3 μm non-LTE emission to a large dataset of PFS limb observations. The final goal, beyond the scope of this paper, is to eventually build a retrieval algorithm to invert the radiances and determine important quantities like CO_2 abundance and non-LTE model collisional parameters, and to derive density and temperature variability of the upper mesosphere and lower thermosphere of Mars. So far, density variations at these altitudes are known with large uncertainties on Mars, the main information coming from model predictions rather than measurements. Some information has been obtained from aerobraking observations at a fixed local time (Theriot et al., 2006) and by the MEx ultraviolet spectrometer SPICAM (Forget et al., 2009; see Bertaux et al., 2006, for description of the SPICAM instrument). However, most data acquired by SPICAM were obtained at night-time, and the diurnal cycle could not be analyzed in detail.

In this paper we present the dataset and inspect the variability of the emerging radiance with respect to the parameters that mostly affect the spectral profile, i.e., altitude, solar zenith angle, season, latitude, local time, and thermal condition of the atmosphere. In a companion paper (Giuranna et al. 2017; part II of the present manuscript), we compare careful selections of PFS measurements to simulated spectra in order to improve non-LTE calculations, provide a more detailed description of the transitions and the non-LTE mechanisms responsible of the observed emissions, and constrain the development of accurate forward models.

This paper will proceed as follows: in Section 2 we present the full dataset of PFS limb observations used in the present work. In Section 3 we describe and identify the main features observed in the PFS spectra at 4.3 μm. The variability of the emission with the tangent altitude is analyzed in Section 4, and the dependence of the non-LTE spectrum on the solar illumination is investigated in Section 5. In section 6 we discuss the variability of the intensity and the height of the peak emission with the season, and how this is associated to the different atmospheric structure and thermal conditions during the year. Finally, we summarize and discuss our results, and present our conclusions (Section 7).

2 - Data set

The Planetary Fourier Spectrometer (PFS) is a two-channels, double pendulum interferometer on board the ESA Mars Express (MEx) spacecraft (Wilson and Chigarro, 2004). It covers the wavenumber range between 200–2000 cm−1 (Long Wavelength Channel, LWC) and 2000–8000 cm^{-1} (Short Wavelength Channel, SWC). Both channels have a sampling step of 1 cm^{-1} and a spectral resolution of 1.3 cm^{-1} (unapodized). Only SWC spectra will be used in this analysis. The instantaneous field of view (IFOV) is 1.52° FWHM (Formisano et al. 2005a; Giuranna et al., 2005a, 2005b). PFS SWC regularly performs limb observations of the strong daytime CO_2 non-LTE emission at 4.3 μm in the atmosphere of Mars. Two main types of limb scanning exist: in one kind, the pointing moves from deep space to the planetary surface (or vice versa), scanning the atmosphere from the top layers to the surface. In the second type, the limb is skimmed tangentially and the pointing moves from deep space to a minimum altitude above the Martian surface, without ever crossing it, and then again to deep space (grazing limb mode).

The PFS limb observations considered in the present analysis were collected over a period that corresponds to more than six Martian years, from January 2004 until December 2016. About 270,000 near-infrared limb spectra were acquired in this period, more than 55,000 of which in the altitude range 0-200 km. A reduced dataset was created for the current analysis. The selection is based on three main criteria: a) only observations with the SZA smaller than 100 degrees are considered, since non-LTE emission is observed up to ~95° SZA (See **Figure 11a** and Section 5 below); b) given the large IFOV of PFS, we selected observations with limited distance between the tangent point and the spacecraft, in order to keep the vertical resolution as high as possible. In particular, we selected observations with IFOV < 45km. The typical IFOV of selected measurements is around 30 km, i.e., ± 15 km with respect to the center of IFOV; c) tangent altitude must be less than 200 km (no emission is observed at higher altitudes on Mars; e.g., Piccialli et al., 2016) and larger than half of the IFOV size plus 5 km (to exclude the planet's surface within the field-of-view). We ended up with about 19,600 observations, covering different seasonal periods and latitudes with different illumination conditions. We note a non-zero radiance level in the PFS spectra acquired above 200 km. This is very likely a residual in the radiometric calibration of the PFS spectra. To correct for this, we collected and averaged more than 3,000 spectra acquired in the altitude range 250-1000 km and subtracted this average spectrum to each single spectrum used in this analysis. As a result, we get a very good zero radiance at 170-200 km (See **Figure 6a**).

In the following we shall discuss the behavior of the non-LTE emission as a function of several parameters. It is therefore important to show what coverage the data set is providing us with. **Figure 1** shows histograms of distribution of PFS limb measurements used in the present analysis for several parameters: a) tangent altitude; b) solar zenith angle; c) latitude; and d) season. Altitude values refer to the center of the IFOV. Although there is a limited number of observations for small values of SZA (< 30°), there are certainly enough measurements to study the behavior of the non-LTE emission for larger values. Indeed, the most interesting range is 30° < SZA < 90°, where most of the variability is expected (López-Valverde and López-Puertas, 1994; Lopez-Valverde et al., 2011b). Altitude coverage is complete, from the troposphere to the upper thermosphere. The latitudinal coverage is also complete, except for the most extreme latitudes (> 70°), and is especially good in the southern hemisphere. The seasonal coverage is relatively uniform and is best during the fall season (180° < Ls < 270°).

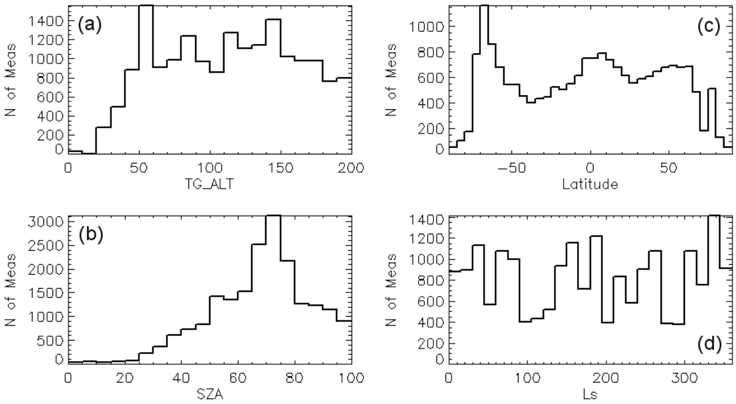

Figure 1. Histograms of distribution of data. (*a*) Tangent Altitude, data bins of 10 km; (b) Solar Zenith Angle, data bins of 5 degrees; (c) Latitude, data bins of 5°; (d) Solar Longitude, data bins of 15°. All values refer to the tangent point. Altitude values refer to the center of the IFOV.

We analyzed the entire dataset described above. In this paper we will only demonstrate PFS measurements acquired during the fall season and in the southern hemisphere (best seasonal and spatial coverage), and in the altitude range 50-200 km. However, similar results and considerations to those that will follow can be extended and applied to the emission spectra observed in the northern hemisphere and during the other seasons.

2.1 – The Zero-Padding technique

The zero-padding (or zero-filling) technique is an interpolation algorithm that increases the number of data points in the spectrum to improve the qualitative spectral features. This algorithm is commonly used in Fourier spectroscopy and a detailed description can be found in Bell (1972). It is known that Discrete Fourier Transform (DFT) only approximates the continuous FT, although it is a very good approximation if used with care. Blind use of DFT, however, can lead to well-known spectral artifacts, such as the picket-fence effect. The picket-fence effect becomes evident when the spectrum contains frequencies which do not coincide with the frequency sample points (Wartewig, S., 2003). If, in the worst case, a frequency component lies exactly halfway between two sample points, an erroneous signal reduction can occur: one seems to be viewing the true spectrum through a picket-fence, thereby clipping those spectral contributions lying between the sampling positions. In practice, the problem does not affect substantially the measured spectrum as far as the spectral components are broad enough to be spread over several sampling positions. The picket-fence effect can be overcome by adding zeros to the end of the interferogram before DFT is performed, thereby increasing the number of points per wavenumber in the spectrum (Bell, 1972; Wartewig, S., 2003). Thus, zero-filling the interferogram has the effect of interpolating the spectrum, reducing the error. As a rule of thumb, one should always at least double the original interferogram size for practical measurements by zero filling it, i.e. one should choose a zero filling factor (ZFF) greater or equal two (Herres and Gronholz, 1984). In those cases, however, where the expected line width is similar to the spectral sample spacing (as, e.g., in the case of non-LTE spectra analyzed here), a ZFF value of up to 8 may be appropriate. An example of the influence of zero filling on the appearance of PFS non-LTE features is demonstrated in **Figure 2**, where we show the original and the zero-filled PFS spectrum around 2336.6 cm^{-1}, the region where the Q-Branch of the first hot (FH) band of the main CO_2 isotope is located (solid green curve in **Figure 4**; see also Figure 6 in Lopez-Valverde et al., 2005). We used the Centimeter–Gram–Second (CGS) system of units for all the radiances shown in this work [erg/(s cm^2 sr cm^{-1})]. While the lines of the original spectrum look badly clipped, the lines are smooth in the zero filled spectrum. It should be noted that zero filling does not introduce any errors because the instrumental line shape is not changed. It is therefore superior to polynomial interpolation procedures working in the spectral domain. For this analysis, we apply zero-padding with a ZFF of 8 to every single PFS spectrum.

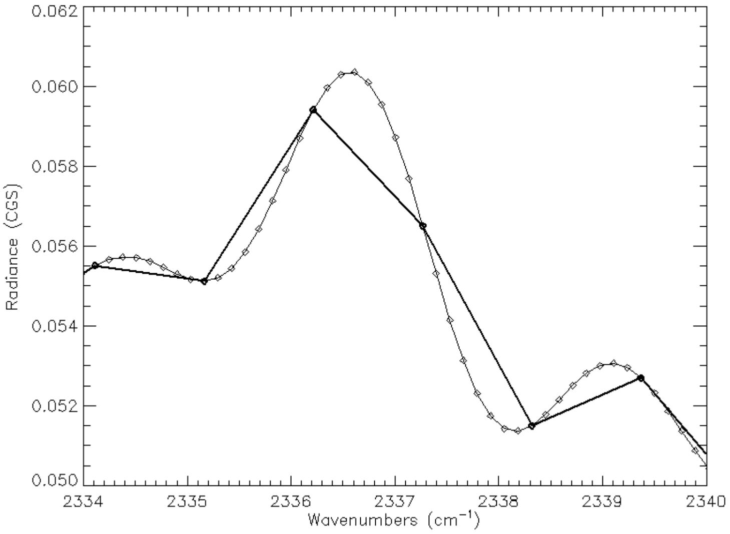

Figure 2. PFS measured spectrum before (thick line) and after (thin line) zero-padding. The ZFF is 8. The Q-Branch of the CO_2 FH band is centered around 2336.6 cm^{-1}.

3 -The 4.3 µm non-LTE emission spectrum

The PFS SWC limb emission spectra between 1.2 and 5 µm are dominated by the CO and CO_2 emission at 4.7 and 4.3 µm, respectively, while CO_2 emission at 2.0 and 2.7 µm, expected to be at least 20 times smaller (Lopez-Valverde et al. 2007), is below the PFS detection level. An example is shown in **Figure 3**. The spectrum displayed corresponds to an average of about 3000 spectra, selected in the 180-270° Ls range in the southern hemisphere (local spring), and for tangent altitudes between 50 and 200 km. The zero-padding technique here applied and the high SNR resulting from the co-addition of may spectra allow the detection of several, weak non-LTE features. None of the features observed in the spectrum of **Figure 3** is due to instrumental noise, but they rather result from one or more transitions between different states and isotopes. Actually, the position and the intensity of the small rotational features (i.e., most of the high-frequency, small-amplitude features in the spectrum of Figure 4) strongly depends on the atmospheric pressures and temperatures, so that the averaging of many spectra, for different altitudes and atmospheric conditions, has the effect to reduce their spectral contrast. The small panel in **Figure 3** shows the spectral region where non-LTE emission of carbon monoxide is observed by PFS. However, this emission will not be discussed in the present work. Hereafter, our attention will be focused to the spectral region 2200-2400 cm^{-1}, that is where the CO_2 non-LTE emission occurs.

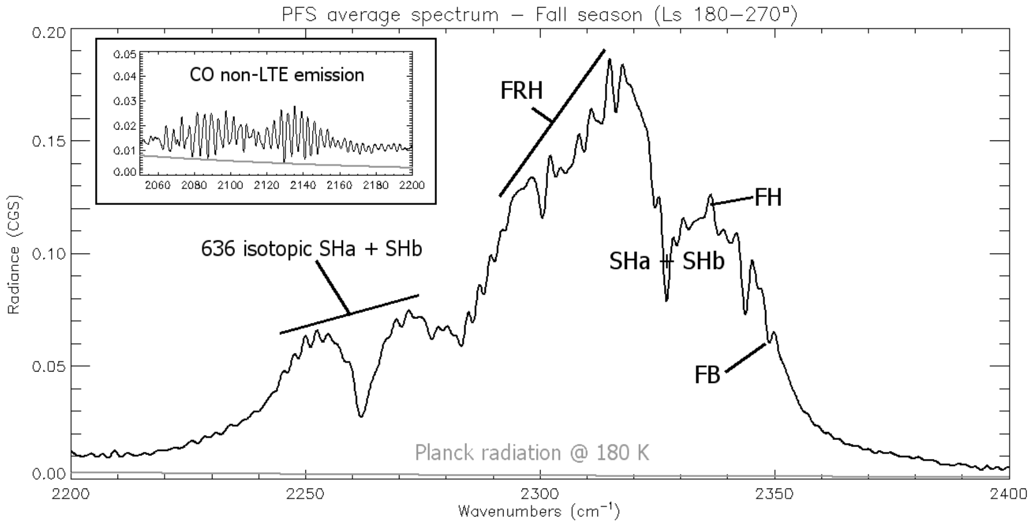

Figure 3. An average of about 3000 PFS limb spectra, selected during the southern spring (180° < Ls < 270°), in the southern hemisphere (latitude < 0°), and for tangent altitudes between 50 and 200 km. Several emission bands can be easily identified in the spectrum. FB, FH, SH, TH, and FRH mean fundamental, first hot, third hot, and fourth hot bands, respectively. The small top-left panel shows the CO emission spectrum at 4.7 μm for the same average. The gray curve is the Planck radiation at 180 K.

A complete identification of all features in the spectrum requires accurate non-LTE theoretical models. Table 1 provides a list of the strongest emission bands of the most abundant CO_2 isotopes in the spectral region of interest. The table has been compiled merging the values extracted from the Appendix of Lopez-Puertas and Taylor (2001) and from the Hitran-2008 database. From an experimental point of view, we can take advantage of the relatively high spectral resolution of PFS to identify the emission bands from their central minima (in the absence of Q-branches) or maxima (when Q-branches are present), which should coincide with column "ν_3" in Table 1. In addition, we use the ALI-ARMS non-LTE code package (Kutepov et al, 1998; Gusev and Kutepov, 2003; Feofilov and Kutepov, 2012; Kutepov et al.,

2017) to isolate the transitions contributing to the measured spectrum in the different spectral ranges. **In Figure 4** we show the main ro-vibrational bands for different isotopologues calculated by the model. Several features related to the main vibrational transitions can be easily identified in the PFS spectrum shown in **Figure 3**. The simulated spectra in **Figure 4** are not intended to be quantitatively compared with PFS observations. Their purpose is to help to understand the contributions of the different bands to the observed spectrum by splitting the simulated spectrum in accordance with the corresponding ro-vibrational bands. The total non-LTE spectrum is given by the sum of all contributing transitions. Solid lines in **Figure 4** are used for the main 626 isotopologue; dashed lines are used for the 636 isotopologue; dotted lines are used for the 628 isotopologue; and the black thin line is for the 627 isotopologue. Moreover, black color in **Figure 4** is used for the fundamental bands (FB, 00011) of the various isotopologues; green color is for the first hot (FH, 01111) bands; and the blue and yellow colors are used for the two strongest second hot bands (SH, 10011 and 10012).

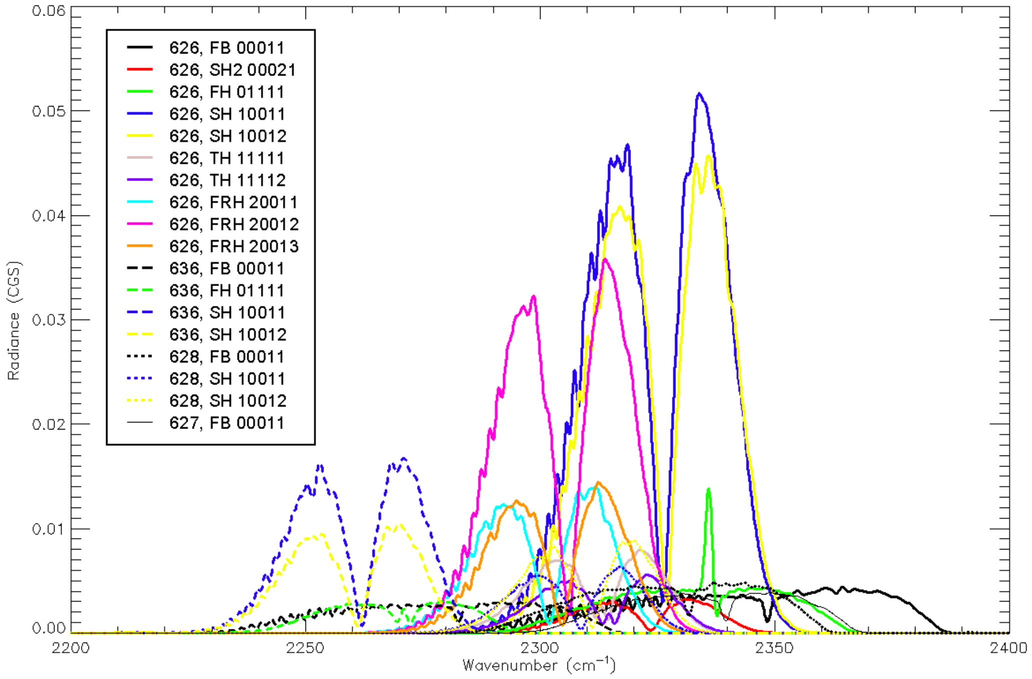

Figure 4. Contribution of different bands and isotopes calculated by the ALI-ARMS non-LTE model, and the corresponding ro-vibrational bands. The transitions are marked by their upper levels using a standard 5 digits notation, and ν_3 transitions in question correspond to changing the 4-th digit by 1 (see also Table 1). Tangent height is 110 km, SZA is 60°. Model calculations were convoluted with the instrument function of PFS SWC (Giuranna et al., 2005b).

The narrow absorption-like feature around 2349.1 $\mathrm{cm^{-1}}$ in the measured spectrum corresponds to the band center of the transition (00011) → (00001) (black solid curve in **Fig. 4**), and is the "fingerprint" of the fundamental band (FB) of the main CO_2 isotope (Table 1). The first hot (FH) band is clearly identifiable as a peak in the measured spectrum around 2336.6 $\mathrm{cm^{-1}}$. This peak is associated to the emission of the Q-branch transition from the state (01111) → (01101) (Tab. 1) and is also clearly visible in the contribution of the FH band as predicted by the model in **Figure 4** (solid green curve). By comparing the measured spectrum in **Figure 3** to the model predictions in Figure 4, we can see that the main contributors in the 2240–2280 $\mathrm{cm^{-1}}$ spectral region are the second hot (SH) transitions of the 636 isotope (blue and yellow dashed curves in **Fig. 4**). The two, quasi-symmetrical lobes associated to the P- and R- branch of these transitions, as well as the minimum around 2262 $\mathrm{cm^{-1}}$ are clearly visible in the PFS average spectrum. Similarly, the main contributors in 2310–2350 $\mathrm{cm^{-1}}$ are the SH transitions of the main isotope (blue and yellow solid curves in **Fig. 4**). For both isotopes, particularly strong are the SH bands labelled as SHa and SHb in Table 1, involving transitions from the states (10011) → (10001) and (10012) → (10002), respectively. A contribution of a third band (SHc) corresponding to the transitions between the levels (02211) → (02201) is also likely present for both isotopes. However, it is one or two order of magnitude less intense (Lopez-Valverde et al., 2005) and cannot be easily recognized in the measured spectra. Finally, the emission in the 2280–2310 $\mathrm{cm^{-1}}$ spectral region is dominated by the fourth hot (FRH) transitions of the main isotope, and particularly those from the (2001x) levels (purple, orange, and cyan solid lines in **Fig. 4**). This is the first clear identification of such bands in the CO_2 non-LTE emission on Mars. A series of relative minima are also clearly visible in the measured spectrum within this spectral range. One can attempt to associate these minima to some of the “ν_3” frequencies reported in Table 1. For instance, the minimum at 2301 cm^{-1} observed in the PFS spectrum could be associated to the (12211) → (12201) FRH band of the main isotope. However, as demonstrated by Kutepov et al. (2017), these absorption features are the result of a very fine combination of lines of emitting and absorbing bands of different isotopes, and depend on the conditions of emission generation and propagation through the atmosphere along the line of sight. Detailed evaluation of “line overlap” is needed to model these features, making the problem relatively complex and computational-time consuming (Kutepov et al., 2017).

A last, puzzling feature is present in the measured spectrum. Namely, the peak centered at 2345.5 cm^{-1}. This feature is clearly seen in experimental spectra at almost all heights, and particularly in the 80–150 km altitude range (see Section 4 below). As one can see from **Figure 4**, the simulated spectra show no separate peaks located in this region. Both HITRAN and HITEMP databases do not reveal any possible transition that might be associated to the features observed by PFS in the 2344–2350 cm^{-1} spectral interval. Our calculations show that even selective variation of the vibrational-vibrational and vibrational-translational rate coefficients involved in non-LTE task cannot increase the pumping of upper levels of transitions, which contribute in this spectral region, to produce a sharp peak there. Kutepov et al. (2017) used complete vibrational-rotational non-LTE analysis to demonstrate that this feature, together with other features present in the spectra, represents the first observational evidence of rotational non-LTE occurring on the atmosphere of Mars.

4- Non-LTE emission as a function of altitude

As anticipated in the previous Section, in this paper we will demonstrate PFS measurements acquired during the fall season (180° < Ls < 270°) and in the southern hemisphere (latitude < 0° N), where have the largest number of measurements (Fig. 2), and thus the best coverage. Note that, in the southern hemisphere, the seasonal range 180–270° Ls actually corresponds to the local spring. In **Figure 5** we show histograms of distribution of data for this season. The vertical resolution of PFS limb observations depends on the distance between the spacecraft and the tangent point. The typical altitude step (i.e., the altitude difference between two consecutive measurements) of most of the PFS limb observations is smaller than 5 km and is peaked around 2 km (**Fig. 5c**). Although the typical IFOV (FWHM) of selected measurements is slightly smaller than 30 km (**Fig. 5d**), the much narrower altitude steps in the considered dataset allow improving the effective spatial (vertical) resolution of PFS limb scans. This technique is known as oversampling and commonly applied in the image and spectra processing (e.g., Nandy et al., 2004). The altitude coverage is complete for the altitude range of our interest (40-200 km) (Fig. 5a), and there is no observation for SZA smaller than ~10° (Fig. 5b). Again, this is not an issue, as most of the variability is expected for 30° < SZA < 90° (López-Valverde and López-Puertas, 1994; Lopez-Valverde et al., 2011b). In particular, we focus in the range between 60° and 80°, where most of PFS data are available.

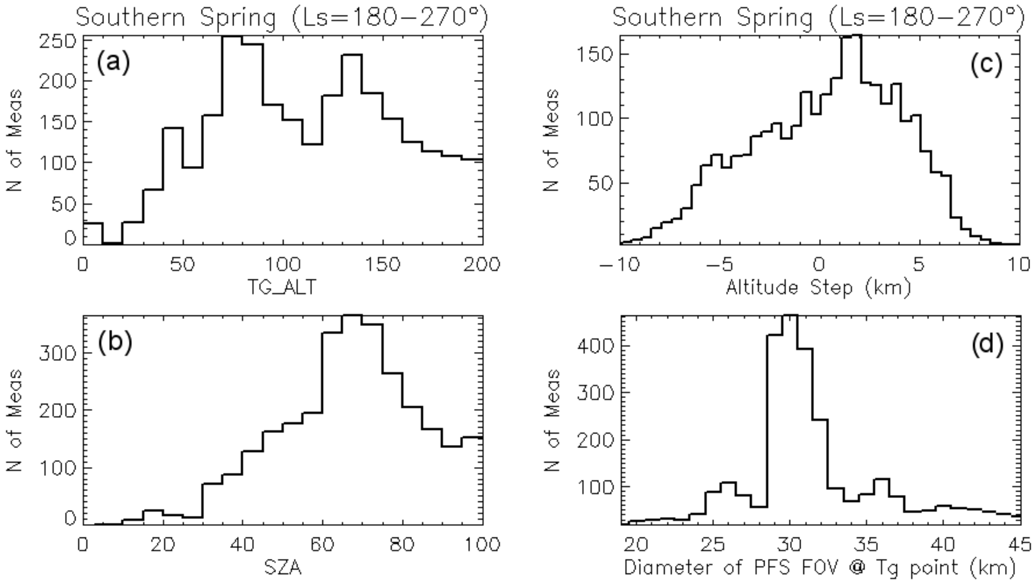

Figure 5. Histograms of distribution of selected data. (*a*) Tangent Altitude, data bins of 10 km; (b) Solar Zenith Angle, data bins of 5 degrees; (c) Altitude step, data bins of 0.5 km. Steps are negative for downward and positive for upward scanning; (d) PFS IFOV (FWHM), data bins of 1 km. Altitude values refer to the center of IFOV.

Figure 6 shows the variation of the CO_2 non-LTE emission spectrum measured by PFS for different altitudes of the tangent point. The same dataset as described above was used here. The PFS spectra were grouped and averaged for bins of 10 km of altitude, from 40 to 200 km (center of IFOV). The selected bin width is approximately the scale height of the Martian atmosphere and is 2-5 times larger than the typical oversampled vertical grid of PFS scans (**Fig. 5c**). This guarantees a sufficient number of measurements for statistical analysis in each altitude bin. In addition, from the PFS Point Spread Function, we can infer that the central 10 kilometers of the PFS IFOV is approximately the altitude range where most of the signal falling into PFS IFOV comes from (see Appendix A).

Only solar zenith angles between 60° and 80° were considered. Since the values of the SZA in the various spectra of **Figure 6** are equally distributed around the average value of 65-70° (see **Fig. 5b**), the tangent altitude can be considered as the key parameter for the various non-LTE emission spectra collected in **Figure 6**, and any change in their shape and intensity can be mainly attributed to the different heights of the observations. The sensitivity of PFS measurements to the oversampled bins of 10 km is also demonstrated by **Figure 6**, where the variations among the averaged spectra are much larger than the instrument noise, even for single measurements (Giuranna et al., 2005).

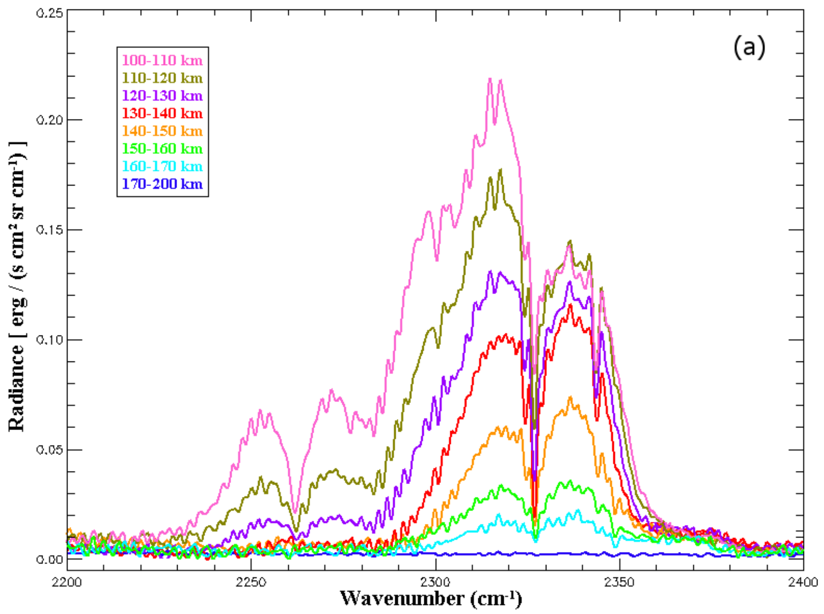
(a)
100-110 km
110-120 km
120-130 km
130-140 km
140-150 km
150-160 km
160-170 km
170-200 km
Radiance [erg / (s cm² sr cm⁻¹)]
0.25
0.20
0.15
0.10
0.05
0.00
2200
2250
2300
2350
2400
Wavenumber (cm⁻¹)

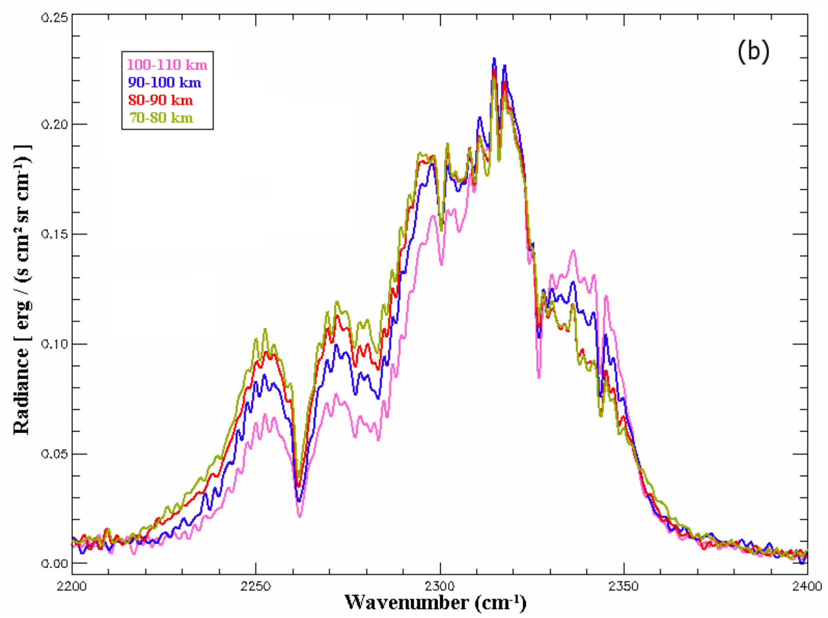
(b)
100-110 km
90-100 km
80-90 km
70-80 km
Radiance [erg / (s cm² sr cm⁻¹)]
0.25
0.20
0.15
0.10
0.05
0.00
2200
2250
2300
2350
2400
Wavenumber (cm⁻¹)

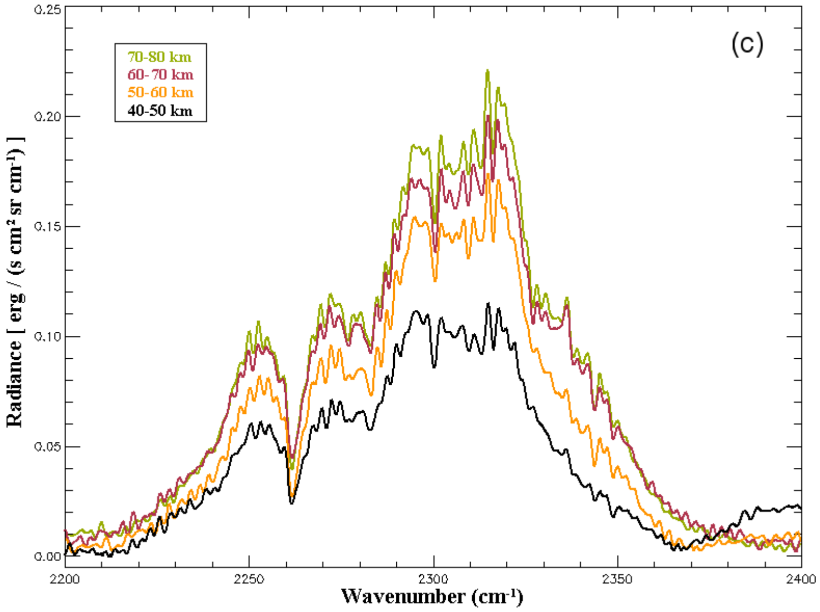

Figure 6. Variation of the CO_2 non-LTE emission spectrum as observed by PFS for different altitudes of the tangent point. The PFS spectra were grouped and averaged for bins of 10 km of altitude, from 40 to 200 km (center of IFOV). See text for more details.

From **Figure 6** we note that no emission is observed for altitudes higher than 170 km. At the highest altitudes (> 150 km, green and cyan curves in **Fig. 6a**), one of the main contribution to the emission spectrum comes from the fundamental band (FB) of the main isotope, whose R-branch can be clearly distinguished in the measured spectrum between 2350-2380 cm^{-1} (**Fig. 6a**). The minimum separating the P- and the R- branches of the FB is also clearly visible around 2349.1 cm^{-1} (see also **Figure 3**, and **Table 1** and the black curve with filled circles in **Figure 4** for a comparison with the models). At these altitudes, the main contribution to the emission spectra comes from the 626 SH bands. It rapidly increases with decreasing altitudes and dominates the emission spectrum, especially in the altitude range 130-170 km (**Fig. 6a**), with its two lobes centered around 2326.9 cm^{-1}. If we compare these two lobes (namely, the P- and R- branches of the 626 SH bands) with the corresponding models in **Figure 4**, we see that they appear much smoother in the data than in the model. As also noted by Lopez-Valverde et al. (2005), this is because the spectral locations of the rotational lines of the 626 SHa and SHc bands (blue and yellow solid curves in **Fig. 4**; see also **Tab. 1** for definitions) are slightly shifted in such a manner that their joint envelope is smoother than for each band separately. Similar considerations apply to the 636 SH and the 626 FRH bands. We note also that, in the considered altitude range (130-170 km), the resulting lobes of the 626 SH bands have slightly different intensities, the R- branch, peaked around 2338 cm^{-1}, being apparently more intense than the corresponding P-branch, peaked around 2318 cm^{-1} (**Fig. 6a**). This apparent asymmetry is due to the contribution of the FB and the first hot (FH, **Figure 3**) band to the total emission. The FH band is clearly identifiable in the spectra as a peak in the measured spectrum around 2336.6 cm^{-1}, whose intensity increases with decreasing altitudes. However, starting from 130 km (violet curve in **Fig. 6a**), we have an opposite situation where the P-branch of the 626 SH bands is apparently more intense than the corresponding R-branch. This asymmetry becomes further evident as the altitude decreases. Moreover, new features appear in the spectra in the 2280–2320 cm^{-1} spectral range. The explanation lies in the (2001x) → (2000x) fourth hot transitions (FRH, **Figure 3**) of the main isotope, which become important for altitudes lower than 130 km (**Figs. 6a**, **6b**, and **6c**) and affect the emission spectrum mainly in the 2280–2320 cm^{-1} spectral range (purple, orange, and cyan solid curves in **Figure 4**). **Figure 6b** shows that, for altitudes lower than 100 km, the contribution of the 626 SH bands becomes less important, and the emission spectrum is dominated by the FRH bands, and by the isotopic 636 SH bands in the 2230-2280 cm^{-1} spectral range (**Figure 3**). The latter are clearly visible in the measured spectra from 40 km up to an altitude of 130 km (violet curve in **Fig. 6a**). The FRH bands and the isotopic 636 SH bands dominate the emission spectra below 80 km (**Fig. 6c**).

The peak emission (i.e., the maximum intensity of the measured spectrum) is observed around 90-100 km (**Fig. 6b**), where several bands sum-up and contribute to the total emission. This is good agreement with previous results by PFS observations (Lopez-Valverde et al. (2011b) and recent results by OMEGA (Piccialli et al., 2016). Lopez-Valverde et al. (2011b) studied the variation of the emission spectrum with altitude through model simulations. They attributed the peak emission observed on Mars around 100 km and at 2317 cm^{-1} as due to the P and R branches of the CO$_2$-626 second hot bands. While, on one hand, PFS spectra shown in **Figure 6** confirm that the peak emission is observed around 100 km, on the other hand they suggest that, at those wavenumbers and altitudes, the contribution of the FRH bands is also important and cannot be neglected.

PFS observations of the 4.3-μm CO$_2$ non-LTE emission collected in the present analysis allow a detailed study of the contribution of the different bands and isotopologues to the emitted spectrum at different altitudes. The results are presented in **Figure 7**. By exploiting the relatively high spectral resolution of PFS we can separately identify the different emission bands from their central minima (in the absence of Q-branches) or maxima (when Q-branches are present). For instance, the contribution of the isotopic 636 SH bands as a function of altitude can be investigated by collecting spectra at different altitudes and measuring the difference of the observed radiance at 2252.5 cm^{-1}, where the P-branch emission is maximum, and at 2261.9 cm^{-1} where the central minimum is located (squares symbols in **Fig. 7b**). In this way we also eliminate a possible, although small, contribution of the FRH bands. Similarly, the variation of the intensity of the FH emission bands as a function of altitude can be characterized by measuring the difference between the radiance of the Q-branch peak emission at 2336.6 cm^{-1} ("$\times_2$" in **Fig. 7b**) and the adjacent continuum which, in turn, is defined by linear interpolation between the two spectral points marked with "$\times_1$" and "$\times_3$" in **Figure 7b**. Similar considerations can be applied to derive the emission profiles of the other bands as a function of altitude, such as the SH bands of the main isotopologue (central minimum at 2326.9 cm^{-1}, triangles in **Fig. 7b**), and the FB (central minimum at 2349.1 cm^{-1}, "+" signs in **Fig. 7b**). The FRH bands can be identified by the strong features (sharp local minima) observed at 2300.9 cm^{-1} and 2136.4 cm^{-1} (diamonds and asterisks, respectively, in **Fig. 7b**).

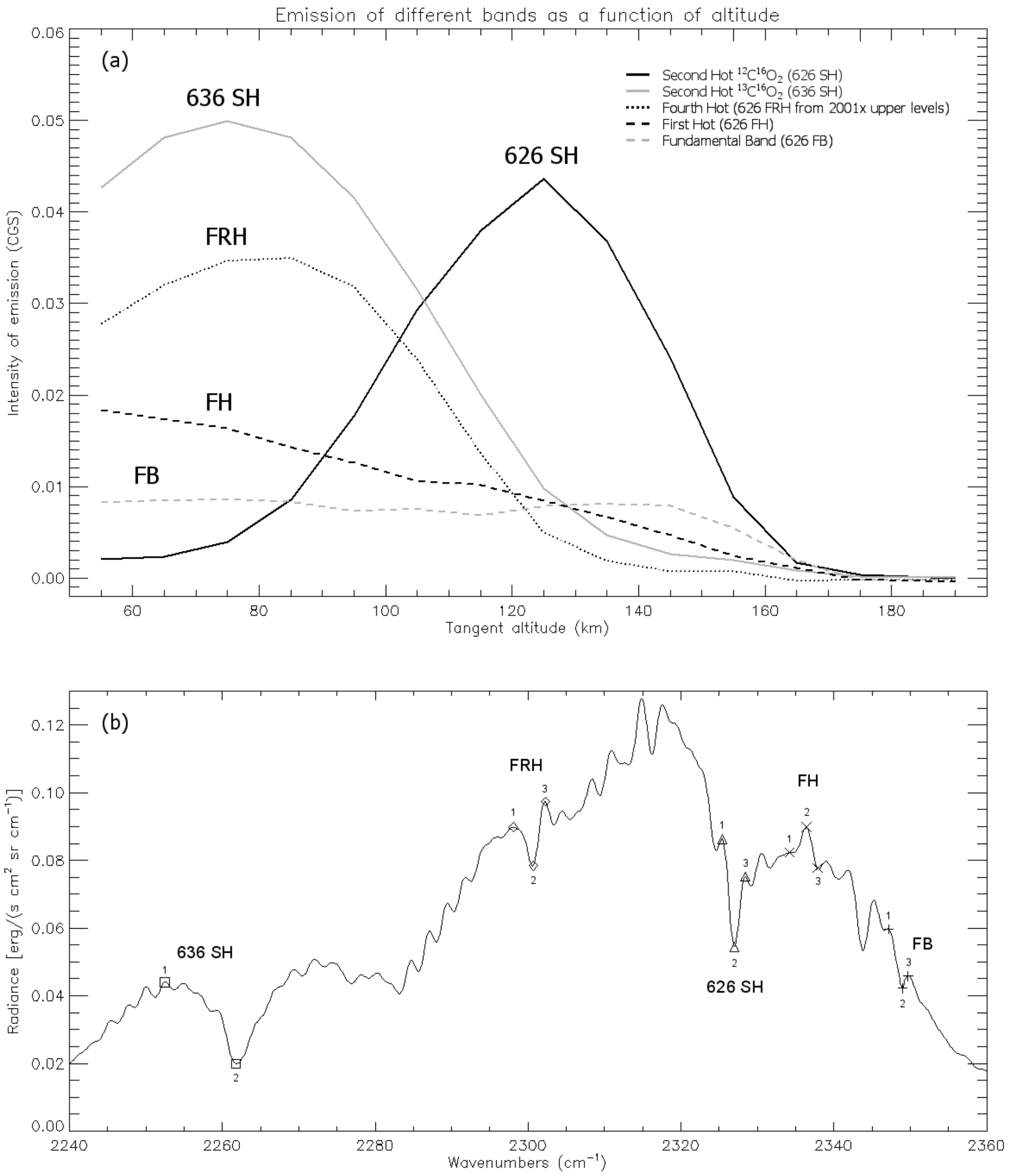

Figure 7. (*a*) Intensity of emission of different bands as a function of altitudes. (*b*) The intensity profiles shown in (*a*) are calculated as follows: $636\_SH = 636\_SH_1 - 636\_SH_2$; $FRH = 0.5\cdot(FRH_1 + FRH_3) - FRH_2$; $626\_SH = 0.5\cdot(626\_SH_1 + 626\_SH_3) - 626\_SH_2$; $FH = FH_2 - 0.5\cdot(626\_SH_1 + 626\_SH_3)$; $FB = 0.5\cdot(FB_1 + FB_3) - FB_2$. Data collected in the southern hemisphere (latitude < 0) and for 180° < Ls < 270° (southern spring). See text for more details.

Figure 7a illustrates the intensities of the various emission bands as a function of altitude. Each band shows its own specific trend and peak altitude. Although the results obtained in each altitude bin may contain information also on nearby altitudes, affecting the absolute value of the average spectra, this will not affect the conclusions in terms of the relative variations with the tangent height obtained in **Figure 7**. Providing the instrument is sensitive enough to measure the variation of the signal between two adjacent bins (i.e., the variation of the signal is larger than the instrument noise, as demonstrated in **Figure 6**), the uncertainty on the altitude is half of the bin size (±5 km in our case). No emission is observed for altitudes higher than 170 km. Note that, although the peak intensity of the emission spectra is observed around 90-100 km (**Fig. 6b**), none of the emission bands here analyzed peaks at that altitude, providing further evidence that different bands are contributing to the total emission, as discussed above. The SH bands of the main isotope show a sharp peak of emission around 120-130 km, and rapidly decrease for higher and lower altitudes. This emission is observed up to a maximum altitude of ~170 km and is the only emission that does not have a significant contribution below 70 km. The isotopic 636 SH bands and the FRH bands exhibit a similar trend. The former is peaked around 70-80 km and the latter show maximum emission between 70-90 km. Among the five bands here analyzed, these two bands have the lowest peak-altitude observed. The main difference between the two is the maximum altitude at which the emission can be observed, namely 130-140 km for the FRH bands, and 150-160 km for the isotopic 636 SH bands. Above the peak altitude, all these bands (namely, the 626 SH, the 636 SH, and the FRH) become optically thin and decrease strongly with tangent altitude, following the exponential decrease in density (**Fig. 7a**). The intensity profile of the FB and the FH bands shows a peculiar trend. Contrary to the previous bands, both are observed at all altitudes between 50 km and 170 km, and show no peak emission. The former is essentially constant at almost all altitudes (50-150 km), and then linearly decreases for higher altitudes. The latter exhibits a linear decrease with increasing altitude for the whole range of altitudes considered.

Commento [MG1]: We moved this part to the Discussion at the end of the manuscript

5- Seasonal and latitudinal variability

In the previous Section we made use of PFS measurements acquired in the southern hemisphere (latitude < 0° N) and during the southern spring season (180° < Ls < 270°) to investigate the CO_2 non-LTE emission of different isotopologues, from different transitions, and as a function of altitude, SZA and local time. Similar results and considerations to those discussed above can be extended and applied to the emission spectra observed in the northern hemisphere and during the other seasons. In this Section we investigate the variation of the non-LTE emission as a function of season (or areocentric longitude, L_S) and latitude. We found that the different illumination conditions due to different seasons and latitudes not only affect the intensity of the non-LTE emission, but also change the altitude at which the maximum emission is observed. The seasonal variation of the altitude and intensity of the peak emission is shown in **Figure 8**. For this analysis we selected observations for all values of tangent altitude and Ls, while the SZA is kept fixed around the value of 60°. The intensity of the emission at 2340 cm^{-1} (directly related to the 626 SH bands) shows a clear cosine-like pattern (**Figure 8b**), which is well correlated with the seasons and the solar flux. The data are best-fitted by the relation $y = a*\cos(Ls + \varphi) + b$ (dashed curves in **Fig. 8**), where y is the measured peak-radiance at 2340 cm^{-1} and a, φ and b are scalar parameters which represents, respectively, the amplitude of the variation, the phase, and the mean value of the peak intensity. The minimum intensity is observed between the aphelion (Ls = 71°) and the southern winter solstice (Ls = 90°), when the solar flux on Mars is at minimum. It then increases in the southern winter and spring seasons, reaches a maximum between the perihelion (Ls = 251°) and the southern summer solstice (Ls = 270°), and decreases again during the southern summer and fall seasons. This behavior is observed in both hemispheres, as a consequence of the fact that the mean solar flux at Mars is about 40% higher around Ls = 240° – 270° compared to Ls = 90°. In **Figure 8a** we show the altitude corresponding to the maximum emission as a function of season. The pattern is similar to that of the intensity. The maximum altitude is observed at the perihelion, at the end of the southern spring (Ls = 270°), where the emission peaks around 120-130 km. This value is well consistent with the results in **Figure 7a**, where the emission of the 626 SH bands during the fall season is well peaked around 120-130 km.

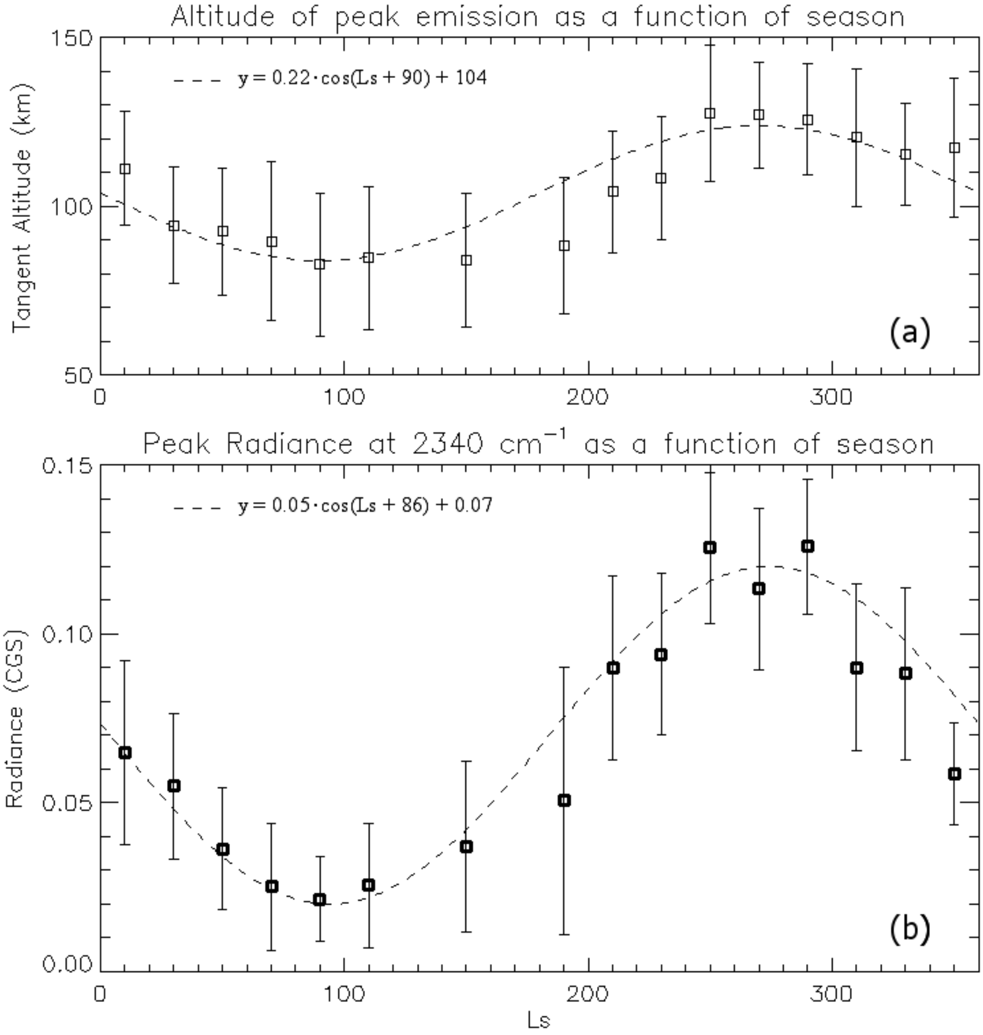

Figure 8. (*a*) Altitude of peak emission at 2340 cm^{-1} as a function of season. Error-bars show the actual PFS IFOV during the measurements (*b*) Intensity of peak emission at 2340 cm^{-1} as a function of season. Data bins of 20° Ls. Error-bars show the standard deviation of the peak intensities for each bin. In both panels, PFS data (squares) are best-fitted by the relation y = a*cos(Ls + φ) + b (dashed curves).

The peak altitude decreases during the southern summer and fall seasons, and reaches a minimum of ~85 km around the southern winter solstice. During the whole southern winter (Ls = 90 – 180°) the altitude of the peak emission stays constant around 80-90 km. It then increases again throughout the southern spring (Ls = 180–270°).

The seasonal variation of the peak altitude observed by PFS is explained by the variability of the thermal structure (scale heights) of the Martian atmosphere with the season, as a response to the changing solar flux. Dayside thermospheric temperature and scale height trends have been recently examined using measurements from the Neutral Gas Ion Mass Spectrometer (NGIMS) and the Imaging Ultraviolet Spectrograph (IUVS) on the Mars Atmosphere Volatile EvolutioN (MAVEN) spacecraft (Bougher et al., 2017). Both instruments confirmed the scale heights decrease after perihelion and reach the lowest value near aphelion, strongly responding to the changing solar flux (Bougher et al., 2017). Forget et al. (2009) used stellar occultations by SPICAM to derive nighttime density and temperature of the upper Martian atmosphere. They found that the periods of minimum and maximum density are, respectively, Ls = 90–120° and Ls = 240–270°, which well correspond to the period of minimum and maximum peak altitude observed by PFS. The mean temperature profiles during the periods of minimum and maximum density appear as they are shifted by 20 km or more (Forget et al. 2009). For Ls = 240–270°, the homopause is observed at an altitude of 120-130 km, while for Ls = 90–120° it is found around 105 km. However, the homopause is observed at essentially the same pressure level in both periods. This is due to the fact that the lower atmosphere is warmer and more expanded during the first period, so that the same altitude does not correspond to the same pressure (Forget et al. 2009). In other words, the altitude of a given pressure level depends on the thermal structure of the atmosphere which, in turn, depends on the season. On the contrary, the pressure level of the peak emission does not depend on the scale heights, as it is mainly controlled by the CO_2 column density above the peak. The seasonal variation of the peak altitude observed by PFS is thus explained by the variability of the thermal structure (scale heights) with the season. The variation in the peak altitude for different seasons or latitudes was already detected by PFS (Formisano et al., 2006). Our results are in agreement with model predictions (Piccialli et al., 2016), according to which the tangent altitude of the peak emission varies with the thermal structure, but the pressure level where the peak of the emission is observed remains constant. Piccialli et al. (2016) also found that seasonal variations of the altitude of constant pressure levels retrieved by SPICAM correlate well with the variations of the OMEGA peak emission altitudes.

In **Figure** 9 we show the latitudinal variation of the intensity of the CO_2 non-LTE emission observed by PFS at 2340 cm^{-1} during the southern spring (Ls = 180–270°) and fall (Ls = 0–90°) seasons. The maximum intensity is observed around the sub-solar latitudes, where the solar flux is maximum. For instance, we know from **Figure 8** that the maximum intensity of the peak emission is observed around Ls = 270°. At this aerocentric longitude the sub-solar latitude is around 25° S. Accordingly, the maximum intensity of the peak emission during the southern spring is observed around 25° S latitude (**Figure 9a**).

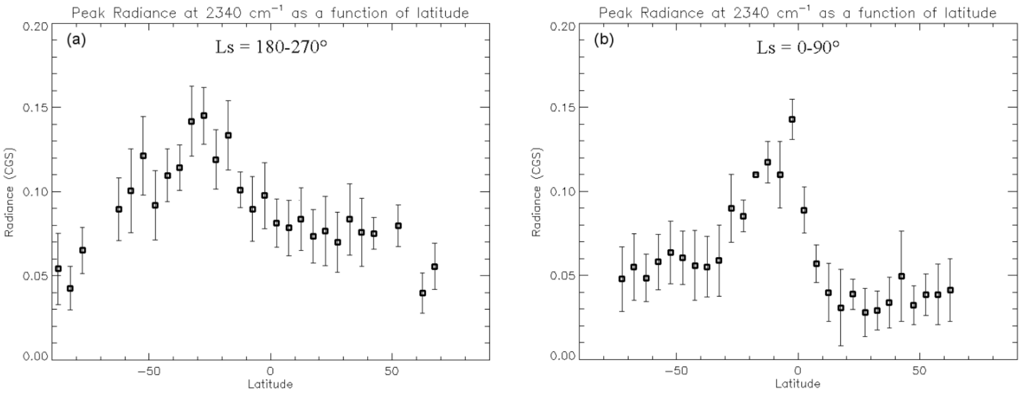

Figure 9. Latitudinal variation of the intensity of the CO_2 non-LTE emission observed by PFS at 2340 cm^{-1} during (*a*) southern spring and (*b*) southern fall seasons. Data bins of 20°. Error-bars show the standard deviation of the peak intensities for each bin.

6- Variations with the Solar Zenith Angle and Local Time

The solar pumping is the main mechanism which triggers the excitation of the CO_2 vibrational levels during daytime in the upper atmosphere. Therefore, one would expect to observe a dependence of the observed radiance with the solar zenith angle.

To analyze the effects of the SZA on the intensity of the non-LTE emission, we used the southern spring dataset described in Section 4 and **Figure 5**. We selected observations for fixed tangent altitudes and varying illumination conditions. Tangent altitude (center of IFOV) is kept fixed around 120-130 km. We further divided the data in morning (LT < 12h) and afternoon (LT > 12h) observations, and then grouped and averaged the selected spectra in bins of 1 degree of solar zenith angle. The results are displayed in **Figure 10**, where we plot the radiance measured at 2340 cm^{-1} (representative of the 626 SH bands emission) as a function of SZA.

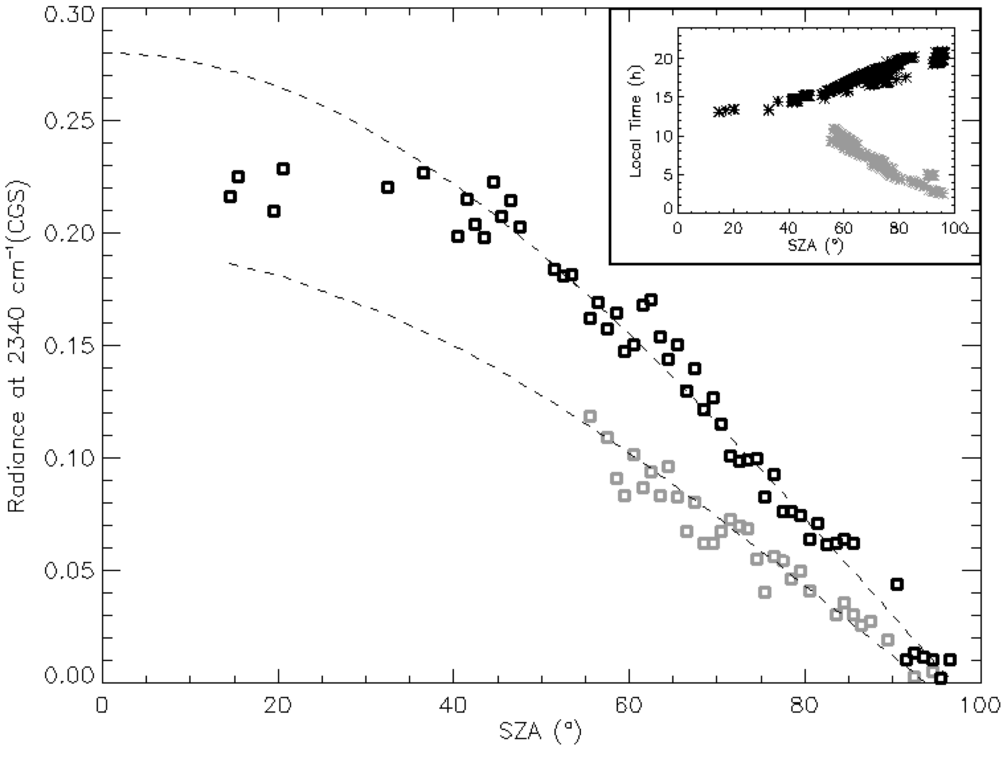

Figure 10. Intensity of the CO_2 non-LTE emission observed by PFS at 2340 cm^{-1} as a function of SZA. Data bins of 1° SZA. Black squares are for afternoon (LT > 12h) and gray squares are for morning (LT < 12h) observations. The small top-right panel shows values of local time as a function of SZA for the selected observations. Data are best-fitted by the relation y = a*cos(SZA) + b (dashed curves).

Non-LTE emission is observed up to SZA ~95°, at the terminator (see also **Figure 11a**). There is a clear dependence of the emitted radiance on the solar incidence angle, which appears to be the dominant parameter affecting the intensity of the non-LTE emission. Between 0 and 40 degrees of SZA the radiance is almost constant, so that the solar incidence angle does not affect substantially the emission. For SZAs larger than 40° the observed emission decreases rapidly with the SZA. Here, the data are best-fitted by the relation $y = a*\cos(\mathrm{SZA}) + b$ (dashed curves in **Fig. 10**), where y is the measured radiance at 2340 cm^{-1} and a and b are scalar parameters. All this follows from emissions dictated by solar pumping. Indeed, we expect the variation due to SZA to be large when large changes in the solar flux occur. However, geometrical path lengths do not vary significantly within the 0-40° range of SZA. This is also in good agreement with previous non-LTE model calculations, which predict small variations of the radiance up to 40°, and acute effects for larger SZAs, especially above 80° (Lopez-Valverde et al., 2007 and 2011). The effects also change with altitude, as a consequence of different competing collisions and solar pumping. Pure cosine variations would only occur higher in the atmosphere, at more tenuous layers.

In the example shown in **Figure 10**, morning observations occur only for SZAs larger than 55°. However, they clearly show an apparent decrease in the intensity of the emission with respect to the observations acquired after the noon. This can be explained by the higher atmospheric temperatures that occur, on average, in the afternoon, and the consequent expansion of the atmosphere. When air heats up, air molecules move faster, pushing each other away and causing air to expand. The opposite occurs when air cools down. This daily process is known as “thermal tides”. The atmosphere expands into a pronounced bulge on the day side of the planet that is up to 30 percent larger than the atmosphere on the night side. This bulge travels around the planet like a tide, hence the name (Zurek et al., 1992; Seiff and Kirk, 1977). In the afternoon, when the atmosphere is warm and expands, the atmospheric layers also expand and move toward higher altitudes. In the morning, the atmosphere is cold and compressed. Thus, sounding different local times at fixed altitudes is somehow similar to sounding different altitudes at fixed local times. In our case, the intensity of the emission at 120-130 km in the morning is less intense than that occurring in the afternoon at the same altitudes, because the atmosphere is compressed, and the same atmospheric layer would be “seen” in the afternoon at higher altitudes, where the intensity of the emission at 2340 cm^{-1} is lower (see **Fig. 6a**). Similarly to the seasonal variation discussed above, the variation of the non-LTE emission with the local time result from variability of the thermal structure of the Martian atmosphere during the day: at different local times, the same altitude does not correspond to the same pressure.

Lowering of the radiance is not the only effect produced by SZA variations. The effect of the SZA on the emission spectrum is shown in **Figure 11**, where we compare different average spectra acquired at 100-110 km at different incidence angles. The spectral shape of the emission spectrum also varies considerably with the SZA. The decrease of the radiance becomes important when one compares the spectra at SZA= 15° and 60° (**Fig. 11a**). Particularly, the drop in the radiance is much larger at 2318 cm^{-1} and 2340 cm^{-1} than at 2295 cm^{-1} or 2255 cm^{-1}. In other words, the radiance decreases much faster in the region of the 626 SH bands than in correspondence of the FRH bands and the 636 SH bands. Actually, the double-peak feature due to the P and R branches of the second hot bands of the main isotope gradually disappears as the SZA increases, as if the contribution of the 626 SH bands is suppressed at such large incidence angles. For SZA larger than 70° the FRH bands dominate the emission spectrum, the 626 SH bands are barely visible, and the intensity of the 636 SH is also decreased by a factor of ~2 compared to SZA = 15°. As anticipated, although very weak, the emission is observed up to SZA ~ 95° (**Fig. 11a**). The average spectrum for SZA = 35° (not shown here) does not appear to be noticeably different from the spectrum for SZA = 15°, again confirming that variations in the incidence angle within 0 and 40 degrees do not affect much the spectral shape and intensity.

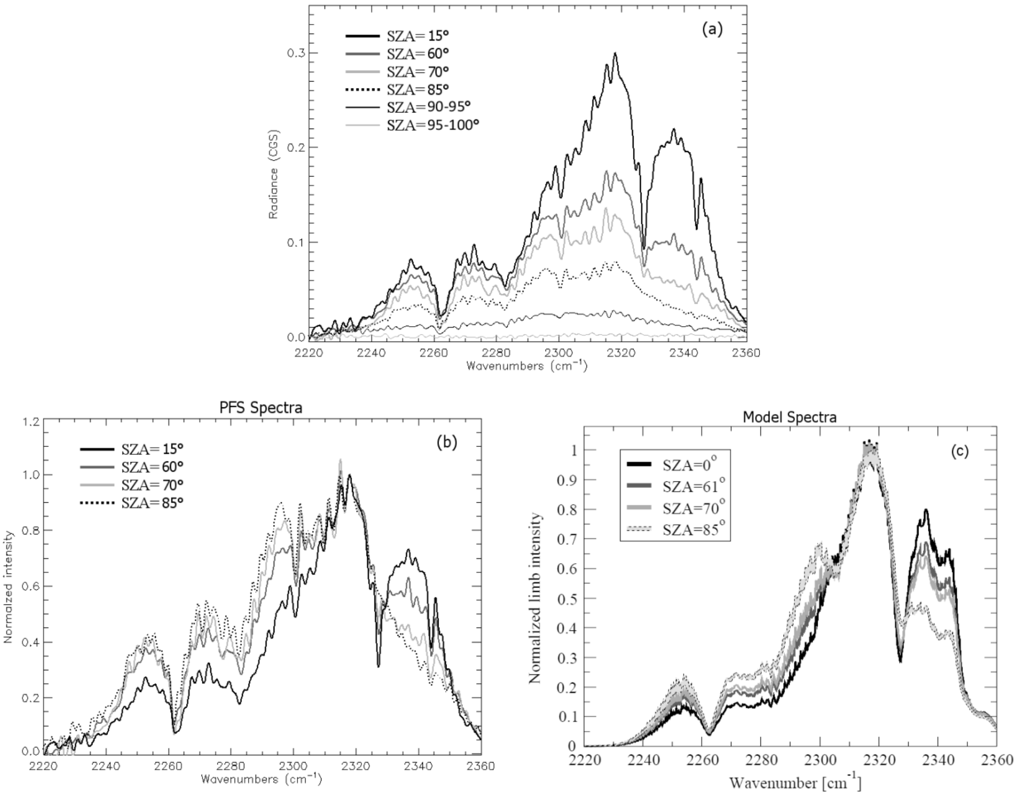

Figure 11. CO_2 non-LTE emission spectra at different SZAs. (*a*) PFS average limb spectra at 100-110 km and for SZA = 15°, 60°, 70°, and 85°. Two average spectra for ranges of 90-95° and 95-100° SZA are also shown. (*b*) Same as above, but normalized to unity at 2318 cm^{-1}. (*c*) Model simulations at 105 km for SZA = 0°, 60°, 70°, and 85° normalized to unity at 2318 cm^{-1}.

The effect of the SZA on the different transitions, bands and isotopes is best seen if **Figure 11b**, where the same spectra as in **Figure 11a** are normalized to unity at 2318 cm^{-1}. It is evident that the relative intensity of the 626 SH bands decreases with respect to the rest of the bands as the SZA increases. On the contrary, the relative contribution of weaker bands and isotopologues, such as the FRH and the 636 SH bands, becomes more important for higher SZAs. A similar behaviour can be recognized in **Figure 11c**, where we plot model predictions of the non-LTE emission at different SZAs. The synthetic spectra shown in **Figure 11c** have been kindly provided for this study by A. Kutepov. The calculations were performed using the ALI-ARMS research code package described in Kutepov et al (1998), Gusev and Kutepov (2003), Feofilov and Kutepov (2012), and adapted to PFS observations (Kutepov et al., 2017). The input atmosphere is set on 0–200 km altitude grid with 1 km vertical step. Vertical profiles of pressure, temperature, volume mixing ratios of atomic oxygen and CO_2, are extracted for the conditions of the PFS observations from the Mars Climate Database v5.2 (Forget et al., 1999; Gonzalez-Galindo et al., 2009; Millour et al., 2015). Synthetic spectra in **Figure 11c** were also normalized to unity at 2318 cm^{-1} to be compared with PFS spectra. The qualitative agreement between models and observation is very good. The simulation is able to describe the observed variability of the spectrum with the SZA. Although the 626 SH bands are still recognizable in modelled spectra at SZA = 85°, their relative intensity is considerably reduced compared to the rest of the bands. Consistently to PFS observations, the model also indicates that the high SZAs make the weaker bands, such as the FRH and the 636 SH bands, relatively more important than the stronger/optically thicker bands.

7- Discussion and conclusion

The new PFS dataset of limb observations, acquired between January 2004 and December 2016, allowed a detailed analysis of 4.3 μm CO_2 non-LTE emission on Mars as a function of several key parameters such as altitude, season, SZA, latitude, and local time. Non-LTE emission is observed up to an altitude of 170 km, and for solar zenith angles as large as 95°. One limit of this dataset is the vertical resolution, the typical radius of the PFS circular field of view being ~15 km. However, this issue was partially overcome, and analyses of emission for different altitudes were performed exploiting the relatively high sensitivity of PFS and by selecting observations with small variations of the tangent heights relative to the center of the IFOV.

Exploiting the relatively high spectral resolution of PFS and the advantage of limb measurements, we identified the main transitions contributing to the observed emission. Previous analyses of observations and theoretical models suggested that it may be necessary to include additional minor hot and isotopic bands in the models, originating from the excitation of higher vibrational levels after the absorption of solar photons between 1 and 2.7 μm, to explain some features observed in the spectra of Mars and Venus, like the asymmetry between the P and R branch of the 626 SH band at 2317 and 2340 cm−1, respectively (Lopez-Valverde et al. 2006; Lopez-Valverde et al. 2007). We found that such asymmetry is due to the contribution of the fourth hot bands of the main isotope, and particularly those from the (2001x) levels. This is the first unambiguous, spectrally resolved identification of such bands, and PFS observations showed that their contribution gradually increases below 140 km, and becomes spectrally dominant for altitudes lower than 100 km.

The different bands and isotopologues identified in the spectra peak at different altitudes, and are observed at different heights. The SH bands of the main isotope show a sharp peak of emission around 120-130 km, and rapidly decrease for higher and lower altitudes. This emission is observed up to a maximum altitude of ~170 km and does not have a significant contribution below 70 km. The isotopic 636 SH bands and the FRH bands are peaked around 70-80 km and 70-90 km, respectively. These are the lowest peak-altitudes emissions observed by PFS. The FRH and the 636 SH bands are observed up to an altitude of 130-140 km and 150-160 km, respectively. Above the peak altitude, all these bands decrease strongly with tangent altitude, following the exponential decrease in density. The FB and the FH are observed at all altitudes between 50 km and 170 km, and show no peak emission. The former is essentially constant up to150 km, and then linearly decreases for higher altitudes. The latter exhibits a linear decrease with increasing altitude for the whole range of altitudes considered in the present analysis (50-200 km).

The vertical profiles shown in **Figure 7** suggest different optical depth and population of the excited vibrational levels between the $^{12}C^{16}O_2$ and the $^{13}C_{16}O_2$

isotopologues at the various altitudes. According to Lopez-Valverde and Lopez-Puertas (1994), all the CO_2 isotopes present similar vibrational populations of the (0,0,v3) states up to about 80 km altitude due to their strong collisional (vibration-vibration) coupling. In the lower mesosphere their simulation suggests that the minor isotopes' excitation is slightly larger than the main isotope, while in the lower thermosphere it is significantly smaller. This is due to the competition between collisions and direct solar pumping, or optical depth. In other words, theoretical models predict that at mesospheric altitudes (below 120 km on Mars), regardless of the slightly different excited level population of the minor isotopes, similar bands of weaker isotopes would emit more (Lopez-Valverde and Lopez-Puertas 1994). For instance, the 636 SH band would give a larger contribution to the spectrum. This is in agreement with the observed trends of 636 SH and 626 SH bands shown in **Figure 7**. Our results may also suggest that the heavier isotopologue tends to concentrate at lower altitudes.

Our results are in good agreement with model simulations and OMEGA observations recently presented in Piccialli et al. (2016). Although the relatively low spectral resolution of OMEGA does not allow identification of most of the emission bands here analyzed, the main 626 and the isotopic 636 SH bands can be certainly discriminated by the OMEGA spectra. Both OMEGA observations and model simulations show negligible contribution of the 626 SH bands below 70 km, in agreement with our results. However, the bump around 120-130 km observed by PFS is only predicted by the model simulations and it is not observed by OMEGA (Piccialli et al., 2016). Similar to our results, the peak emission of the isotopic 636 SH bands is observed around 80-90 km both in OMEGA data and model predictions. Above the peak, the 636 SH bands are optically thin and decrease strongly with tangent altitude (Piccialli et al., 2016).

For a fixed altitude, the solar zenith angle (SZA) is the main parameter affecting the intensity and the spectral shape of the non-LTE emission. For SZA between 0 and 40 degrees the intensity of the emission does not show significant variations. For

SZAs larger than 40° the observed emission decreases rapidly with increasing SZA, following a cosine-like relation. However, lowering of the radiance is not the only effect produced by increasing SZAs. The different illumination also affects the spectral shape of the emission or, in other words, the relative contributions from different CO_2 bands. In particular, high incidence angles tend to increase the relative contribution of weaker bands compared to stronger/optically thicker bands. This is partially explained by the different dependence of the solar pumping on the SZA for different levels, whose 4.3 um bands contribute to limb signal. For instance, 2.7 μm bands, pumping levels 10011 and 10012 of 626 SH bands, are the strongest ones and are getting quicker exhausted with increasing SZA/decreasing altitude compared to the analogous, much weaker bands and levels of the 636 isotopologue. However, additional simulations with theoretical models are necessary for a complete explanation. Indeed, also contributors at 4.3 μm may be relevant. SZA/altitude dependence of pumping sources reflects of how the opacity in these short wavelength bands is varying. To explain the observed variations in the spectra, the variation of contributions of various 4.3 μm transitions must also be considered, since these contributions depend both on pumping and individual weighting functions along the passes. For a fixed SZA, we found apparent variation in the intensity of the emission for different local times. This is in response to the daily variations of the atmospheric thermal structure (thermal tides). In the afternoon, when the atmosphere is warm and expands, the atmospheric layers also expand and move toward higher altitudes. In the morning, the atmosphere is cold and compressed. Thus, sounding different local times at a given altitudes is similar to sounding different altitudes at a given local time.

The intensity and the altitude of the maximum emission also change with the season, and are largely correlated to changes of the solar flux. For the 626 SH bands, the maximum altitude is observed at the perihelion, at the end of the southern spring, where the emission peaks around 120-130 km. The peak altitude then decreases during the southern summer and fall seasons, and reaches a minimum of ~85 km around the southern winter solstice. This is explained by the variability of the thermal structure of the Martian atmosphere with the season, as a response to the changing solar flux. The altitude of a given pressure level depends on the thermal structure of the atmosphere which, in turn, depends on the season. On the contrary, the pressure level of the peak emission does not depend on the scale heights, as it is mainly controlled by the CO_2 column density above the peak. Latitudinal variation of the intensity of the CO_2 non-LTE are also investigated. The maximum intensity is observed around the sub-solar latitudes, where the solar flux is maximum.

With their unprecedented spatial and temporal coverage, and relatively high spectral resolution, PFS dayside limb observations provide an extremely valuable dataset for the analysis of the 4.3-μm CO_2 non-LTE emission in the atmosphere of Mars. Exploiting the large amount of information contained in it, this dataset could eventually allow retrieval of temperatures and densities in the mid and upper atmosphere of Mars. However, not before a complete forward model will be developed and successfully used to fit the observed emission spectra. The vertical resolution of PFS limb observations can be significantly improved for a substantial part of the scans, relying on the small step of vertical scanning and the overlapping of many measurement. Indeed, the majority of the limb scans allow application of standard de-convolution routines (e.g., Rajan et al., 2003; Nandy et al., 2004; Roscoe and Hill, 2001) to refine the altitude resolution of measurements, keeping it acceptable (not more than a few km, according to current estimates) for effectively retrieving pressure and temperature profiles in the mid and upper atmosphere.

The present results, while on one hand confirm certain aspects of the non-LTE emission modelling, on the other hand provide new challenges for the models.

Acknowledgements. The authors cordially thank Alexander Kutepov, Artem Feofilov, and Ladi Rezac for providing us the synthetic spectra used in this analysis, and for a very helpful discussion on the non-LTE problem. The PFS experiment has been built at the Istituto di Astrofisica e Planetologia Spaziali (IAPS) (former IFSI, Istituto di Fisica dello Spazio Interplanetario) of Istituto Nazionale di Astrofisica (INAF), and has been founded by the Italian Space Agency (ASI) in the context of the Italian participation to the ESA's Mars Express Mission. Since May 2013, MG is the PI of the PFS experiment, originally lead by VF. PFS data are publicly available via the ESA Planetary Science Archive.

PW is supported by the UPWARDS project, funded from the European Union's Horizon 2020 research and innovation programme under grant agreement No. 633127. GS is supported by the Italian Space Agency (ASI) under the agreement 2016-23-H.0.

Appendix A

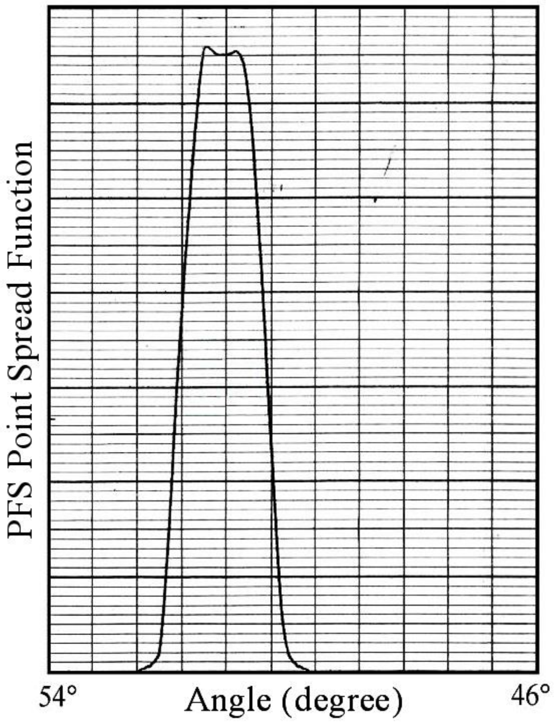

Figure A1. The PFS Point Spread Function measured in the laboratory. Note the steepness of the function and the plateau on the top.

References

Bell, R.J. (1972), "Introductory Fourier Transform Spectroscopy", Academic Press, New York.

Bertaux, J.-L., et al. (2006), SPICAM on Mars Express: Observing modes and overview of UV spectrometer data and scientific results, J. Geophys. Res., 111, E10S90, doi:10.1029/2006JE002690.

Bougher, S. W., et al. (2017), The structure and variability of Mars dayside thermosphere from MAVEN NGIMS and IUVS measurements: Seasonal and solar activity trends in scale heights and temperatures, J. Geophys. Res. Space Physics, 122, 1296–1313, doi:10.1002/2016JA023454.

Feofilov, A. G. and Kutepov, A. A.(2012), Infrared Radiation in the Mesosphere and Lower Thermosphere: Energetic Effects and Remote Sensing, Surv. Geophys, 33, 1231–1280, doi:10.1007/s10712-012-9204-0.

Forget, F., Hourdin, F., Fournier, R., Hourdin, C., Talagrand, O., Collins, M., Lewis, S.R., Read, P.L., Huot, J.-P. (1999), Improved general circulation models of the martian atmosphere from the surface to above 80 km, J. Geophys. Res., 104, E10, 24155-24176.

Forget, F., F. Montmessin, J.-L. Bertaux, F. Gonzalez-Galindo, S. Lebonnois, E. Quémerais, A. Reberac, E. Dimarells, and M. A. Lopez-Valverde (2009), Density and temperatures of the upper Martian atmosphere measured by stellar occultations with Mars Express SPICAM, J. Geophys. Res., 114, E01004, doi:10.1029/2008JE003086.

Formisano, V., and 47 coauthors (2005a), The Planetary Fourier Spectrometer (PFS) onboard the European Mars Express mission. Planet. Space Sci. 53, 963-974.

Formisano, V., and 15 coauthors (2005b), A Martian PFS average spectrum: Comparison with ISO SWS, Planet. Space Sci. 53, 1043-1052.

Formisano, V., Maturilli, A., Giuranna, M., D’Aversa, E., L´opez-Valverde, M. A. (2006), Observations of non-LTE emission at 4.5 microns with the planetary Fourier spectrometer aboard the Mars Express mission, Icarus, 182, 51-67.

Gilli, G., M. A. López-Valverde, P. Drossart, G. Piccioni, S. Erard, and A. Cardesín Moinelo (2009), Limb observations of CO_2 and CO non-LTE emissions in the Venus atmosphere by VIRTIS/Venus Express, J. Geophys. Res., 114, E00B29, doi:10.1029/2008JE003112.

Gilli, G., M. A. López-Valverde, B. Funke, M. López-Puertas, P. Drossart, G. Piccioni, and V. Formisano (2011), Non-LTE CO limb emission at 4.7μm in the upper atmosphere of Venus, Mars and Earth: Observations and modeling, Planet. Space Sci., 59, 1010–1018, doi:10.1016/j.pss.2010.07.023.

Gilli, G., M. A. López-Valverde, J. Peralta, S. Bougher, A. Brecht, P. Drossart, and G. Piccioni (2015), Carbon monoxide and temperature in the upper atmosphere of Venus from VIRTIS/Venus Express non-LTE limb measurements, Icarus, 248, 478–498, doi:10.1016/j.icarus.2014.10.047.

Giuranna, M., Formisano, V., Biondi, D., Ekonomov, A., Fonti, S., Grassi, D., Hirsch, H., Khatuntsev, I., Ignatiev, N., Malgoska, M., Mattana, A., Maturilli, A., Mencarelli, E., Nespoli, F., Orfei, R., Orleanski, P., Piccioni, G., Rataj, M., Saggin, B., Zasova, L. (2005a), Calibration of the Planetary Fourier Spectrometer long wavelength channel. Planet. Space Sci. 53(10), 993–1007.

Giuranna, M., Formisano, V., Biondi, D., Ekonomov, A., Fonti, S., Grassi, D., Hirsch, H., Khatuntsev, I., Ignatiev, N., Malgoska, M., Mattana, A., Maturilli, A., Mencarelli, E., Nespoli, F., Orfei, R., Orleanski, P., Piccioni, G., Rataj, M., Saggin, B., Zasova L. (2005b). Calibration of the Planetary Fourier Spectrometer long wavelength channel. Planet. Space Sci., Volume 53, issue 10, 993–1007.

González-Galindo, F., F. Forget, M. A. López-Valverde, M. Angelats i Coll, and E. Millour (2009), A ground-to-exosphere Martian general circulation model: 1. Seasonal, diurnal, and solar cycle variation of thermospheric temperatures, J. Geophys. Res., 114, E04001, doi:10.1029/2008JE003246..

Gusev, O., and Kutepov, A. (2003), Non-LTE Gas in Planetary Atmospheres. ASP Conference Series, Vol. 288, 318-330.

Herres, W., and J. Gronholz (1984), Understanding FT-IR Data Processing, Part 1: Data Acquisition and Fourier Transformation, Comp. Appl. Lab. 4, 216, 1-5.

Kutepov, A., Gusev, A., Ogibalov, P. (1998), Solution of the non-LTE problem for molecular gas in planetary atmospheres: superiority of Accelerated Lambda Iteration. J. Quant. Spectrosc. Radiat. Transfer, Vol. 60, No. 2, 199-220.

Kutepov, A. A., Rezac, L., and Feofilov, A. G. (2017), Evidence of a significant rotational non-LTE effect in the CO_2 4.3 μm PFS-MEX limb spectra, Atmos. Meas. Tech., 10, 265-271, doi:10.5194/amt-10-265-2017.

Lellouch, E., Encrenaz, T., de Graauw, T., Erard, S., Morris, P., Crovisier, J., Feuchtgruber, H., Girard, T., Burgdorf, M. (2000), The 2.4 - 45 μm spectrum of Mars observed with the Infrared Space Observatory, Planet. Space Sci., 48, 1393-1405.

Lopez-Puertas, M., Lopez-Valverde, M.A. (1995), Radiative energy balance of CO_2 non-LTE infrared emissions in the martian atmosphere, Icarus, 114,113-129.

Lopez-Puertas, M., Taylor, F. W. (2001), Non-LTE radiative transfer in the atmosphere, World Scientific, Series on atmospheric oceanic and planetary physics, vol. 3, Singapore.

Lopez-Valverde, M.A., Lopez-Puertas, M. (1994), A non-local thermodynamic equilibrium radiative transfer model for infrared emissions in the atmosphere of Mars. 2: Daytime populations of vibrational levels, J. Geophys. Res. E, 99, 13117-13132.

Lopez-Valverde, M.A., Lopez-Puertas, M., Lopez-Moreno, J.J., Formisano, V., Grassi, D., Maturilli, A., Lellouch, E., Drossart, P. (2005), Analysis of CO_2 non-LTE emission at 4.3 μm in the martian atmosphere as observed by PFS/Mars Express SWS/ISO, Planet. Space Sci. 53, 1079.

Lopez-Valverde, M.A., Garcia-Comas, M., Drossart, P., Formisano, V. (2006), Progress in modelling non-LTE radiative processes on Mars, Second workshop on Mars atmosphere modelling and observations, Granada, Spain. Edited by F. Forget, M.A. Lopez-Valverde, M.C. Desjean, J.P. Huot, F.Lefevre, S. Lebonnois, S.R. Lewis, E. Millour, P.L. Read and R.J. Wilson.Publisher : LMD, IAA, AOPP, CNES, ESA, 2006., p.613.

Lopez-Valverde, M.A., Drossart, P., Carlson, R., Mehlman, R., Ross-Serote, M. (2007), Non-LTE infrared observations at Venus: from NIMS/Galileo toVIRTIS/Venus Express, Planet. Space Sci., 55, Issue 12, 1757-1771.

Lopez-Valverde, M.A., Sonnabend, G., Sornig, M., Kroetz, P. (2011a), Modelling the atmospheric CO_2 10- μm non-thermal emission in Mars and Venus at high spectral resolution, Planet. Space Sci., 59, 999-1009.

Lopez-Valverde, M.A., Lopez-Puertas, M., Funke, B., Gilli, G., Garcia-Comas, M., Drossart, P., Piccioni, G., Formisano, V. (2011b), Modeling the atmospheric limb emission of CO_2 at 4.3 μm in the terrestrial planets, Planet. Space Sci., 59, 988-998.

Maguire, W. C., J. C. Pearl, M. D. Smith, B. J. Conrath, A. A. Kutepov, M. S. Kaelberer, E. Winter and P. R. Christensen (2002), Observations of high-altitude CO_2 hot bands in Mars by the orbiting Thermal Emission Spectrometer, Journal of Geophysical Research, vol. 107, NO. E9, 5063, doi: 10.1029/2001JE001516.

Millour E, Forget F, Spiga A, Navarro T, Madeleine JB, Montabone L, Pottier A, Lefevre F, Montmessin F, Chaufray JY, Lopez-Valverde MA, Gonzalez-Galindo F, Lewis SR, Read PL, Huot JP, Desjean MC, MCD/GCM development Team (2015), The Mars Climate Database (MCD version 5.2). European Planetary Science Congress 2015, held 27 September - 2 October, 2015 in Nantes, France, Online at http://meetingorganizer.copernicus.org/EPSC2015/EPSC2015-438.pdf.

Nandy P., Smith J.L, Decker M.L. (2004), Subpixel resolution with the multispectral thermal imager (MTI), Proceedings Volume 5159, Imaging Spectrometry IX; doi: 10.1117/12.509759

Piccialli, A., M. A. López-Valverde, A. Määttänen, F. González-Galindo, J.Audouard,F.Altieri,F.Forget, P. Drossart, B. Gondet, and J. P. Bibring (2016), CO_2 non-LTE limb emissions in Mars' atmosphere as observed by OMEGA/Mars Express, J. Geophys. Res. Planets, 121, 1066–1086, doi:10.1002/2015JE004981.

Seiff, A., and D. B. Kirk (1977), Structure of the atmosphere of Mars in summer mid-latitudes, J. Geophys. Res., 82, 4364–4378.

Rajan D., Chaudhuri S., Joshi M.V. (2003), Multi-Objective Super Resolution: Concepts and Examples, IEEE Signal Processing Magazine, 20, 49-61.

Roscoe H.K. and J.G.T. Hill (2001) Vertical resolution of oversampled limb-sounding measurements from satellites and aircraft, J. Quant. Spectrosc. Radiat. Transfer, 72, 237–248.

Theriot, M., G. Keating, R. Blanchard, S. Bougher, R. Zurek, R. Tolson, J. Murphy, F. Forget, and J. Bertaux (2006), Interannual Comparison of Temporal and Spatial Structure in the Martian Thermosphere from Atmospheric Accelerometer Measurements of Mars Reconnaissance Orbiter (MRO) during Aerobraking and Stellar Occultation Measurements from the SPICAM Ultraviolet Infrared Atmospheric Spectrometer of Mars Express (MEX), in AAS/Division for Planetary Sciences Meeting Abstracts, vol. 38, p. 73.02.

Wartewig, S. (2003), IR and Raman spectroscopy : fundamental processing. Wiley-VCH, Weinheim, Great Britain.

Wilson, A. and A. Chicarro (2004) Mars Express: the scientific payload. Ed. by Andrew Wilson, scientific coordination: Agustin Chicarro. ESA SP-1240, Noordwijk, Netherlands: ESA Publications Division, ISBN 92-9092-556-6, XIV + 216 pp.

Zurek, R. W., J. R. Barnes, R. M. Haberle, J. B. Pollack, J. E. Tillman, and C. B. Leovy (1992), Dynamics of the atmosphere of Mars, in Mars, pp. 835– 933, Univ. of Ariz. Press, Tucson.